Supporting Information

Ultra-broadband and Omni-directional Perfect Absorber based on Copper Nanowire/Carbon Nanotube Hierarchical Structure

Fatemeh Kiani[1], Florian Sterl[2], Ted V. Tsoulos[1], Ksenia Weber[2], Harald Giessen[2], Giulia Tagliabue[1]*

[1] *Laboratory of Nanoscience for Energy Technologies (LNET), IGM-STI, EPFL, 1015 Lausanne*

[2] *4th Physics Institute and Research Center SCoPE, University of Stuttgart, Pfaffenwaldring 57, 70569 Stuttgart, Germany*

**E-mail: giulia.tagliabue@epfl.ch*

19 pages, 14 figures, 1 table

Contents

S1. Growth Methodology

S1.1 Hierarchical Cu-CNT NWs arrays structure

A copper foil (99.9%, 0.250 mm thick, Alpha Aesar) was first cut into 1*1 cm^2 specimens and adequately cleaned by immersion into diluted (1M) aqueous hydrochloridric acid (HCl) for 2 min, followed by sequential rinsing in acetone, isopropanol, and DI water to remove the native oxide layer on the surface and organic contaminants. After the substrate was dried with N_2 flow, it was placed directly onto an alumina boat which was then inserted into an open horizontal CVD quartz tube furnace (CARBOLITE). Then, the furnace temperature was slowly increased to 450℃ under static air at a heating rate of 10 K/min and the CuO NWs were directly grown on the surface of Cu substrates by air-annealing for 4h at isothermal condition. After the growth, the furnace was cooled down naturally to room temperature at a cooling rate of ~5 K/min to prevent any delamination of the oxide layer on the Cu substrate. The detailed procedure that we followed for CuO NWs growth was reported previously.[1] To make the obtained nanowires catalytically-active for the growth of CNTs, the as-grown CuO NWs were reduced to Cu NWs by a hydrogen thermal treatment. At first, the reaction chamber was evacuated to a base pressure of 4.0×10^{-5} Torr, cleaned by cyclic gas purging and backfilled with Ar (99.999% in purity) with a flow rate of 300 sccm to remove other gases. Then, the temperature of the furnace was raised at a rate of ~15 K/min from room temperature to 350℃ under Ar atmosphere. After attaining to this temperature, a high purity Ar/H_2 gas mixture (300 sccm Ar/30 sccm H_2) was blown into the chamber for 10 min, and CuO NWs were reduced into Cu NWs with the least morphological change of nanowires structure. The optimized condition for obtaining Cu NWs was found using ref.[2-4] Finally, to efficiently grow CNTs on the thermally-reduced Cu NWs catalysts, at first, the H_2 supply was stopped and the furnace temperature was raised from 350℃ to 600℃ at a heating rate of 30 K/min in Ar atmosphere. Once the temperature reached to 600℃, acetylene (C_2H_2) gas was blown into the chamber as the carbon precursor at a flow rate of 40 sccm while keeping the same Ar flow at atmospheric condition. After 10 min growth of CNTs on Cu NW arrays, the C_2H_2 supply was stopped and the system was rapidly cooled down to room temperature at a rate of ~30 K/min under Ar cover to prevent oxidation and also to avoid collapse of the nanowire structure at elevated temperatures. As Cu NWs can easily be collapsed and sintered by annealing at elevated temperatures (>400℃) in Ar and H_2 atmospheres[2-4] and as acetylene decomposition occurs at 600℃,[5] the entire CNT growth process was performed in just a short period of time. The optimum condition for the growth of CNTs on Cu NWs was found using ref.[3,5] Figure S1 shows the EDS elemental mapping and spectrum for a single Cu-CNT nanowire structure. Figure S2 shows high-magnification SEM images of an individual Cu-CNT NW at two different magnifications.

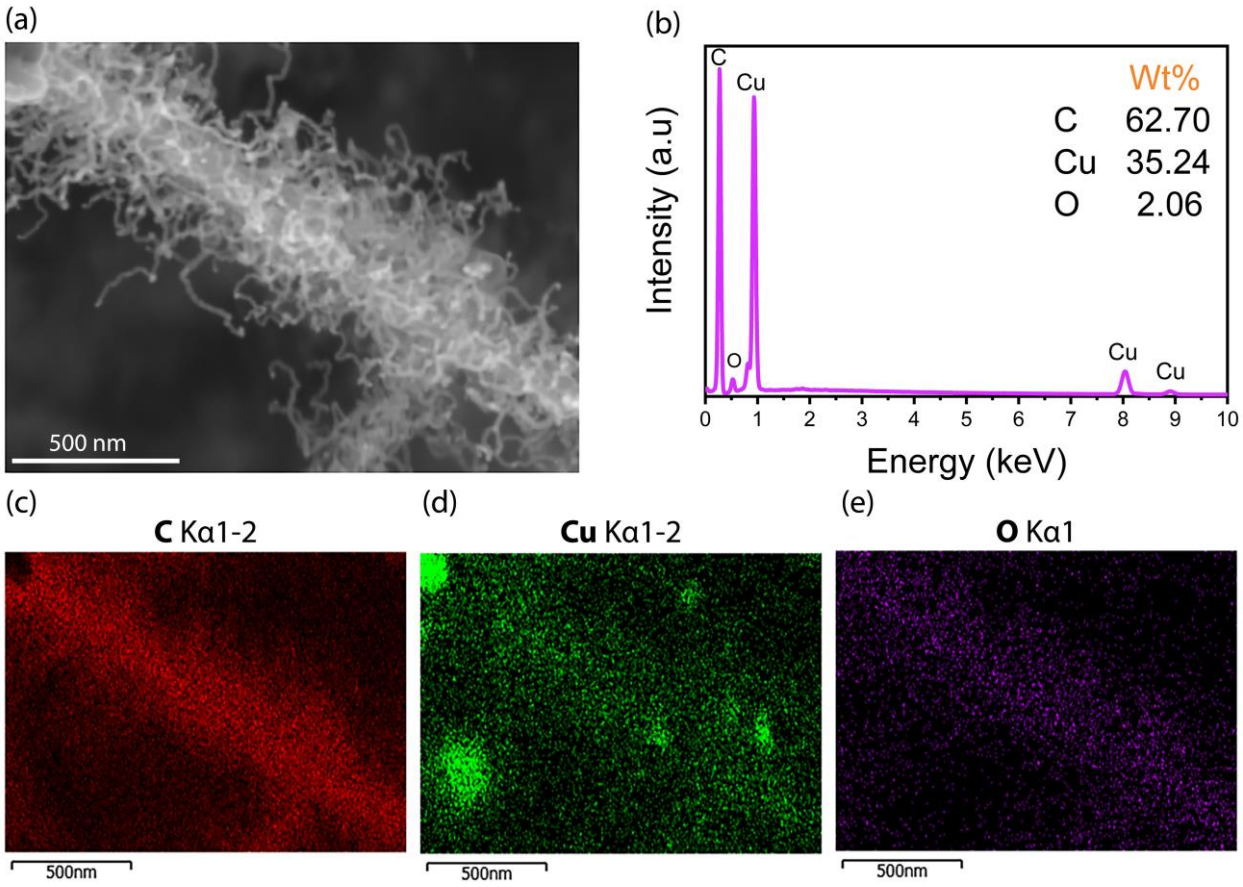

Figure S1. Elemental mapping results obtained from the region of a single Cu-CNT NW. (a) electron micrograph, (b) Energy-dispersive X-ray spectroscopy (EDS) spectrum, and (b) EDS mapping of carbon, copper, and oxygen elements of the corresponding scanned area for a single Cu-CNT NW.

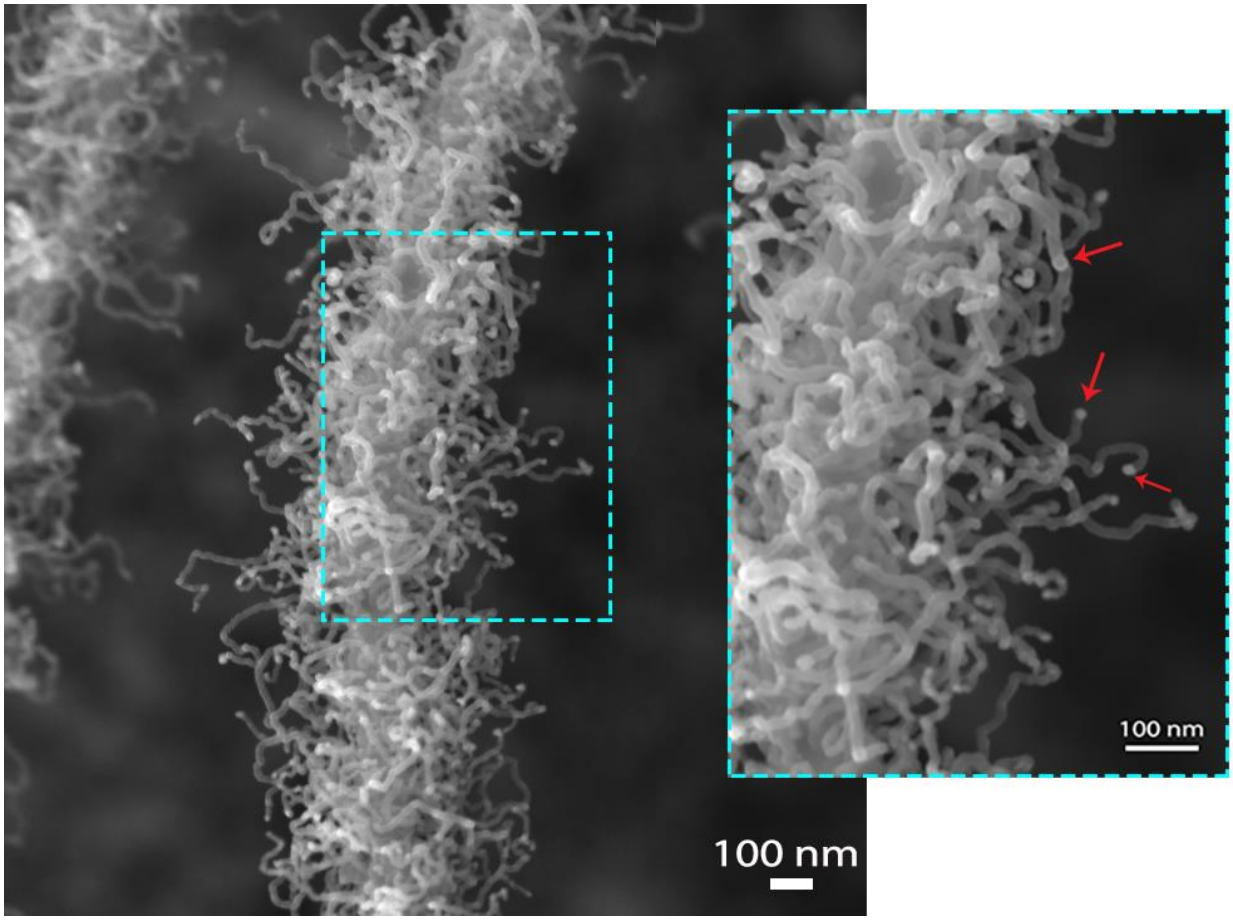

Figure S2. High-magnification SEM images of a typical Cu-CNT nanowire at two different magnifications, indicating size, shape, and growth mechanism of CNTs. The SEM system was ZEISS Gemini SEM 300 in the in-lens mode.

S1.2 Collapsed Cu-C structure

For comparison purposes, a similar procedure to the one introduced in section S1.1 was evaluated for growth of CNTs on Cu NWs arrays by using methane gas (300 sccm Ar/40 sccm CH_4) as the carbon precursor with a much higher decomposition temperature of 900℃ to show the effect of growth temperature on the resulting structure and the necessity of using acetylene gas for fabricating Cu-CNT NWs structures. By considering the high decomposition temperature of methane, as all the heating and cooling stages were performed at rates similar to the ones used in the CVD process by using acetylene gas, the Cu NWs arrays were exposed to the damaging Ar atmosphere at elevated temperatures for a much longer time. Figure S3 shows top-view SEM images of the resulting collapsed Cu-C structure.

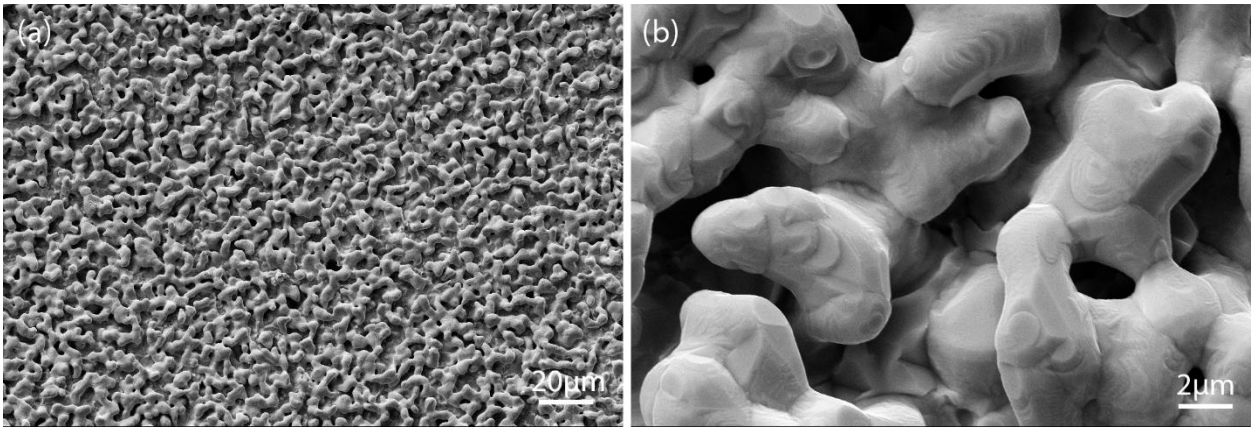

Figure S3. Top-view SEM images of the collapsed Cu-C structure obtained by using methane gas as the carbon precursor at two different magnifications.

S1.3 Cu NW array structure

The Cu NWs arrays structure was obtained by H_2 thermal reduction of a thermally-grown CuO NWs structure at a similar condition to those reported in section S1.1 for obtaining the Cu NWs before CVD growth of CNTs, followed by rapid cooling under Ar cover. The optimized condition for thermal reduction of CuO NWs into Cu NWs was found using ref.[2-4] Figure S4a depicts a tilted-view SEM image of the obtained Cu NWs arrays, indicating that the nanowire morphology is well preserved after the H_2 thermal treatment.

S1.4 CuO thin film

The CuO thin film was grown by thermal oxidation of a Cu substrate at 400℃ for 4h where the growth of CuO NWs is suppressed.[6] To grow the CuO thin film structure, all the process were carried out in a similar condition to those reported in section S1.1 for the CuO NW growth except the oxidation temperature. Figure S4b shows a tilted-view SEM image of the obtained CuO thin film, visualizing its granular surface texture.

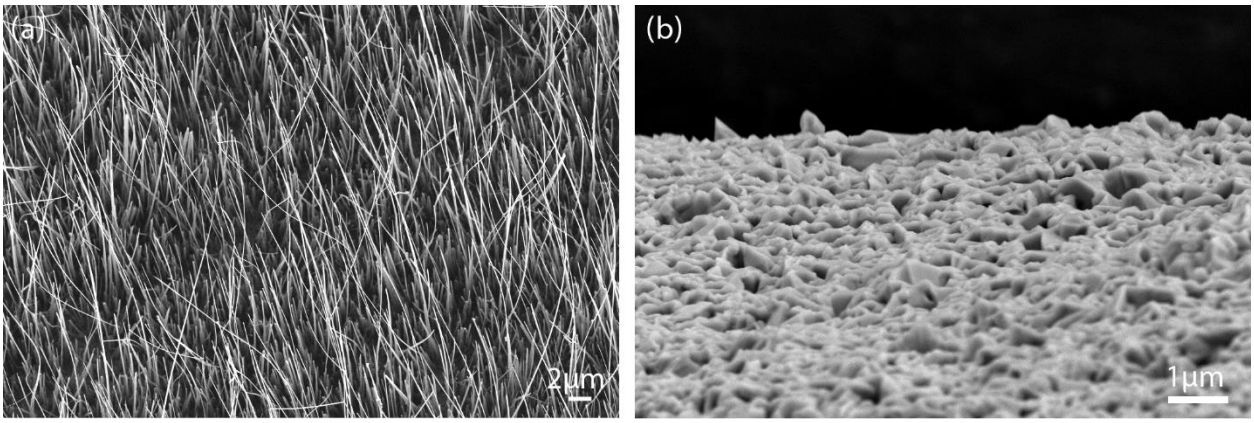

Figure S4. Tilted-view SEM images of (a) thermally-reduced Cu NWs arrays and (b) the thermally-grown CuO thin film on the Cu substrate.

S2. Reflectance measurements

Two independent optical measurement set-ups were used to measure the reflectance of the structures across the broad 0.4-10μm specular range. The experimental setup used to measure the wavelength-resolved reflectance of the structures in the Vis-to-NIR region (400-1000nm) was based on an inverse microscope (Nikon Eclipse TE2000-U) in combination with an imaging spectrometer (Princeton Instruments SP2500i) equipped with a Peltier-cooled 2D CCD detector (Princeton Instruments PIXIS 256, Figure S5). A 100x, 0.9 NA objective (Nikon TU Plan Fluor) was used in order to access a wide range of angles. The image generated by the microscope was projected onto the entrance slit of the spectrometer or onto an RGB imaging camera via a 4-f setup, which gives access to an intermediate Fourier plane. By replacing the second lens of the 4-f setup with a lens of half the focal distance, this lens acted as an imaging lens for the intermediate Fourier plane, so that the Fourier plane instead of the image plane could be imaged onto the detector/camera.[7]

To record reflectance spectra as a function of the incident angle, a specialized Köhler illumination path was constructed. A fiber-coupled broadband, high-intensity, laser-driven light source (Energetiq EQ-99) was focused onto a pinhole (diameter 400 μm). The image of the pinhole was directly projected into the back focal plane (BFP) of the objective, which is conjugated to the Fourier plane. Illuminating a small spot in the BFP corresponds to a narrow range of incident angles on the sample. As the fiber and the pinhole were mounted on an XY translation stage, the position of the pinhole and thus the position of the spot in

the BFP could be adjusted in order to vary the incident angle from normal incidence to approximately 64 degrees (limited by the objective NA).

Figure S6 shows typical Fourier space images taken with the RGB imaging camera (see Figure S5). This camera was used to determine the range of incident angles, and to adjust the illumination to a certain incident angle by moving the X,Y stage. Figure S6a displays the Fourier space image obtained by illuminating a diffusive surface, so that light is scattered into the full NA of the objective. This image was used to determine the position and the diameter of the NA in the camera image. To obtain normal incidence, the diffusive surface was replaced by a mirror and the resulting image of the pinhole was moved into the center of the Fourier plane (Figure S6b). The diameter of this image corresponds to an incident NA of approximately 0.12, or a maximum incident angle of approx. 6.9 degrees. Figure S6c depicts the Fourier plane image for an average incident angle of 48 degrees. In this case, the incident NA ranges from approx. 0.63 to 0.85, corresponding to an angle range of approximately 38 degrees to 58 degrees.

The access to the intermediate Fourier plane was employed to distinguish specular from diffuse reflectance. An iris was placed on an XY translation stage to serve as an aperture stop (A-stop). If the A-stop was left open, the objective collected all the radiation reflected and/or scattered into the full NA of the objective for a certain incident angle. If the A-stop was closed and moved into position by imaging the reflectance from a mirror (as in Figure S6b,c) until its diameter matched the diameter of the illumination spot in the BFP, all diffuse reflectance was blocked and thus only the specular component arrived at the spectrometer.

All measured reflectance spectra were normalized to the (specular) reflectance of a silver mirror (ThorLabs, PF10-03-P01) and multiplied by the known reflectance of silver. However, since the measured signals were very low, the back reflection from the microscope objective had to be taken into account as well. This was measured by simply recording an empty sample plane. The reflectance of the sample can then be quantified as

$$R_{sample} = \frac{I_{sample} - I_{air}}{I_{mirror} - I_{air}} R_{mirror} \qquad \text{(S-1)}$$

where I denotes the measured intensity in counts and R is the relative reflectance.

At infrared wavelengths (2-10µm), the reflectance measurements were performed with an optical set-up consisting of a Fourier-transform infrared (FTIR) spectrometer (Bruker Vertex 80) and an infrared microscope (Hyperion 2000) with a 36X, 0.5 N.A. objective. The data were normalized to a gold mirror

reference sample. All of the above optical measurements were repeated for five different positions of each sample and were averaged over the five values.

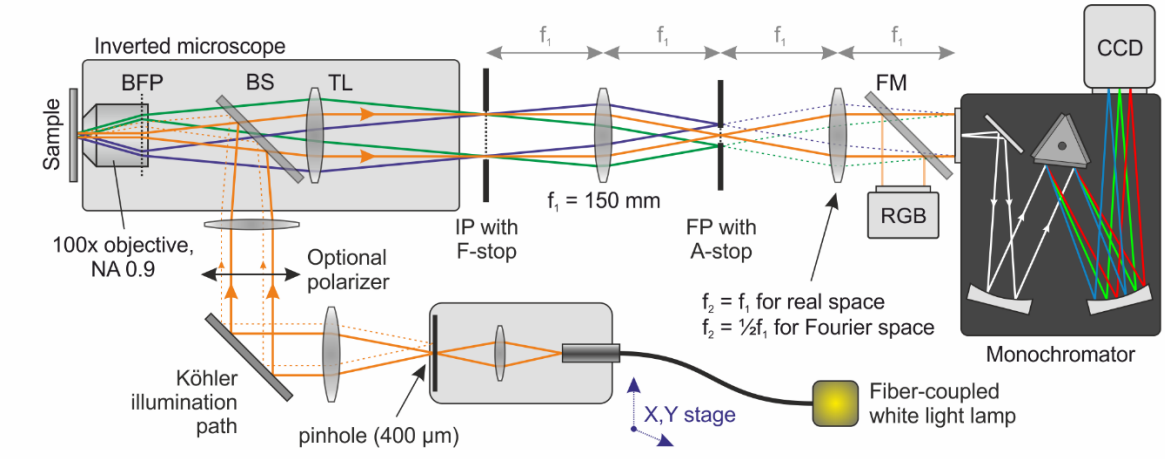

Figure S5. Experimental setup for angle-resolved reflectance spectroscopy in the Vis-to-NIR region. BFP = Back Focal Plane, BS = Beam Splitter, TL = Tube Lens, FM = Flip Mirror, IP = Image Plane, F-stop = Field Stop, FP = Fourier Plane, A-stop = Aperture Stop.

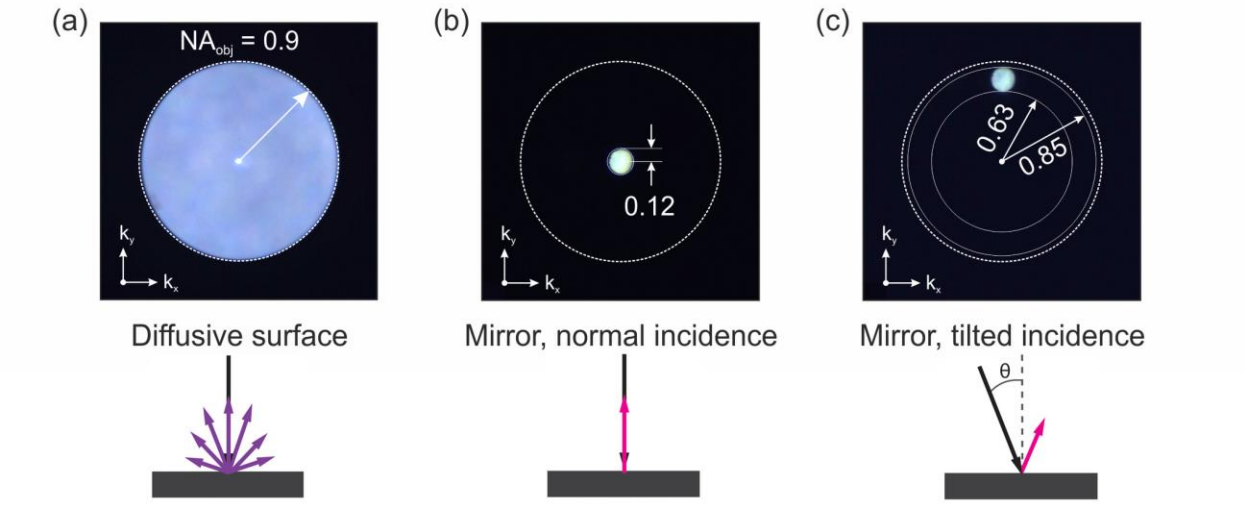

Figure S6. k-space images of a diffusive sample (a) and of a mirror at normal (b) and tilted incidence (c), together with their corresponding schematics depicting the illumination conditions (black arrow - incidence angle) and the collected reflectance component (pink arrow – specular reflection and purple arrow– diffuse reflection).

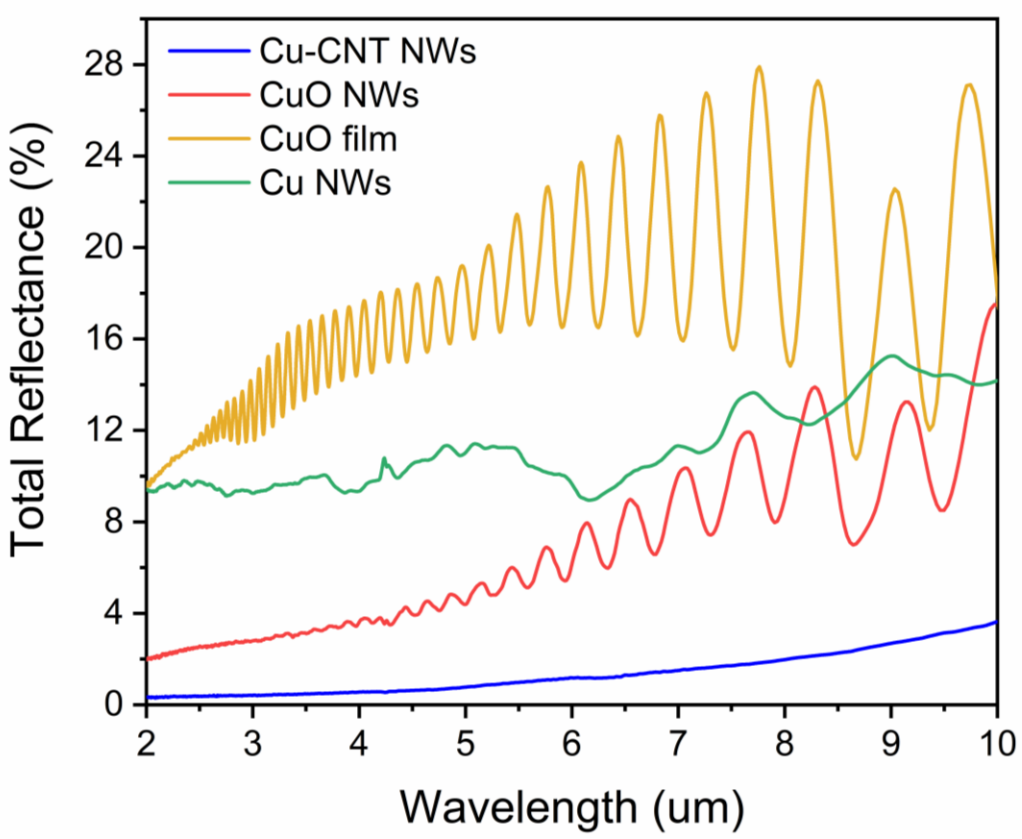

Figure S7. Total reflectance spectra of the CuO NWs, CuO thin film, Cu NWs, and Cu-CNT NW arrays structures at normal incidence across the mid-infrared range of the spectrum.

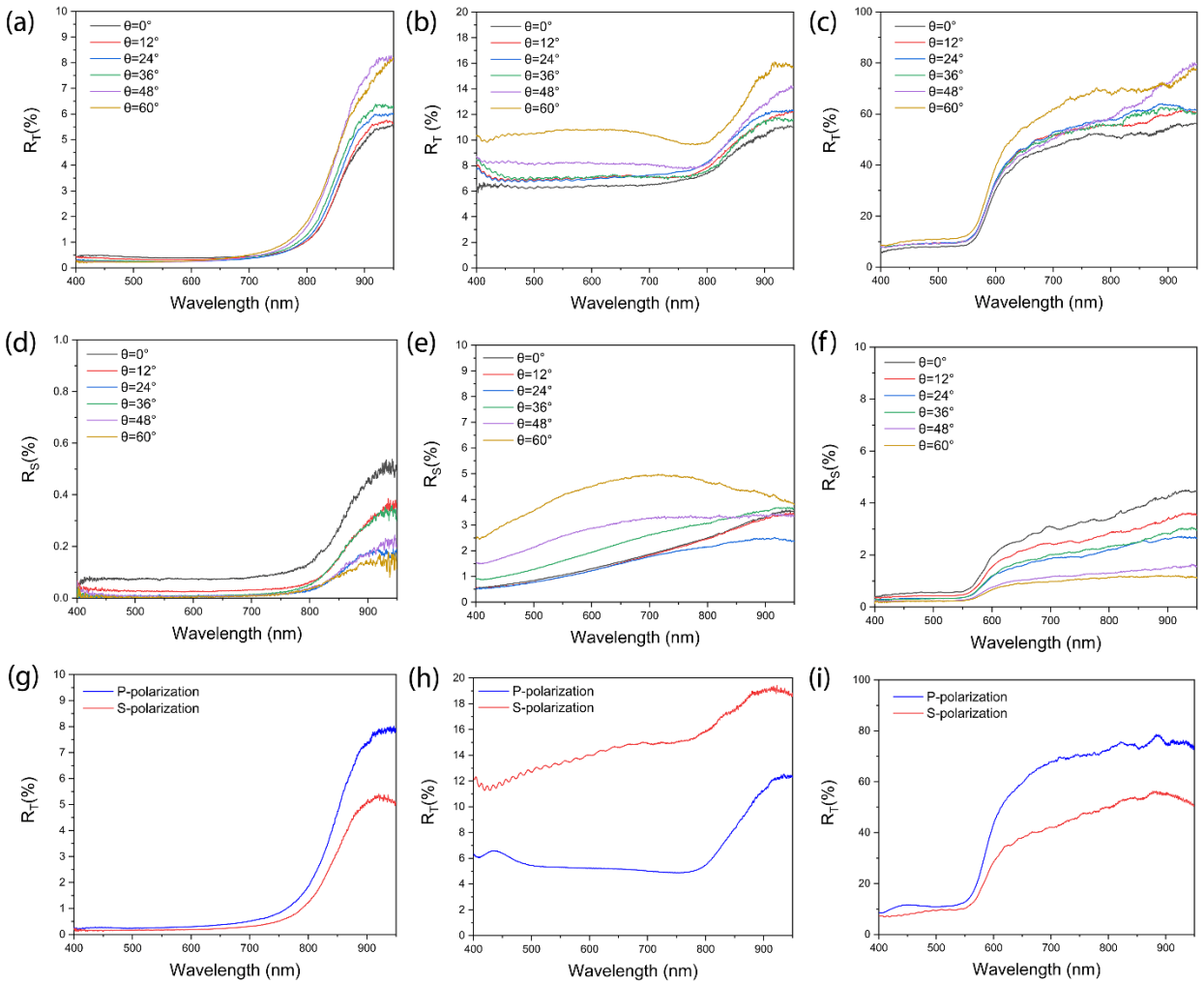

Figure S8. Experimental reflectance measurement results for CuO NWs, CuO thin film, and Cu NW samples in the Vis-to-NIR range. Angle-resolved total reflectance spectra of the (a) CuO NWs, (b) CuO thin film, and (c) Cu NW samples. Angle-resolved specular reflectance spectra of the (d) CuO NWs, (e) CuO thin film, and (f) Cu NW samples. Total reflectance spectra of the (g) CuO NWs, (h) CuO thin film, and (i) Cu NW samples under s- and p-polarized lights at 50° incident angle.

S3. Modeling and simulation

S3.1 Effective medium approximation

Considering the subwavelength dimensions of the constituent elements (Cu NWs and CNTs) of our hierarchical structure, to simulate the reflectance spectra of an individual Cu-CNT NW as well as a dense forest of Cu NWs or Cu-CNT NWs, an effective medium approximation was used.[8] The effective relative permittivity can be calculated knowing the volume fraction of each component in a nanocomposite as well as its optical properties. For a two-material system we have the following rule of mixtures:

$$\varepsilon_{eff} = f_1\varepsilon_1 + (1 - f_1)\varepsilon_2 \quad \text{(S-2)}$$

where f denotes the volume fraction and ε is the relative permittivity. To get an idea of volume fractions and size of features in each of our structures, analysis of SEM images was performed by imageJ software. Figure S9 shows the results of the image analysis for a typical Cu-CNT NW and a CuO NWs arrays structure. As evident from the close-up view SEM image in Figure S9a, radially-grown CNTs on each individual Cu NW in the structure have different lengths, meaning that the effective relative permittivity should be graded along the thickness of the CNTs coating. Accordingly, we divided the overall CNT layer into two segments, each of 107nm thickness, and, after binarizing the SEM image to black and white areas, we determined the volume fractions of air and CNT for each segment. For statistical purposes we repeated the analysis on three different SEM images and obtained the following average compositions of the two EMLs:

$$\varepsilon_{eff(EML1)} = 0.25\varepsilon_{CNT} + 0.75\varepsilon_{air} \quad \text{(S-3)}$$

$$\varepsilon_{eff(EML2)} = 0.65\varepsilon_{CNT} + 0.35\varepsilon_{air} \quad \text{(S-4)}$$

As describe in the modelling section, these optical properties were applied to the two 107nm-thick films that coated an individual 100nm-diameter Cu NW.

For modeling the effective relative permittivity of the Cu-CNT NWs arrays structure, we followed a similar image analysis procedure. We assumed that no major morphological change occurred in the NWs structure during the CNT growth process. Therefore, image analysis was performed on an SEM image of a vertically-aligned CuO NWs arrays structure (see Figure 2b). The same air and NW volume fractions were then used to describe both the Cu NWs and the Cu-CNT NWs forests. The overall thickness of the NWs layer is approximately 30 μm. However, due to the presence of wires of different lengths, at different heights a different NW density can be observed. We thus divided the overall NWs layer into five EMLs,

each with different volume fractions of air and NWs, as depicted in Figure S9b and Table S1. For the Cu NW forest, the permittivity of the i-th layer, $\varepsilon_{eff,i}$, can be obtained with the expression:

$$\varepsilon_{eff,i} = f_{NW,i}\varepsilon_{Cu} + (1 - f_{NW,i})\varepsilon_{air} \quad \text{(S-5)}$$

Finally, for calculating the effective relative permittivity for each EML in the forest of Cu-CNT NWs, we took into account the calculated effective relative permittivity for the EMLs equivalent to the CNT coating (eq. S.3 and S.4) as well as their volume fractions considering 30 μm and 100nm for the length and diameter of the underlying Cu NW. We thus obtained the following relation for the Cu-CNT NWs arrays structure:

$$\varepsilon_{eff,i} = f_{NW,i}(0.036\varepsilon_{Cu} + 0.32\varepsilon_{eff(EML1)} + 0.65\varepsilon_{eff(EML2)}) + (1 - f_{NW,i})\varepsilon_{air} \quad \text{(S-6)}$$

Figure S9c shows the simulated real part of the refractive index profile across the five EMLs of the Cu-CNT NWs structure at three different wavelengths. According to the analytical Fresnel equation, the reflection at normal incidence is defined as,[9]

$$R = \left|\frac{n_1 - n_2}{n_1 + n_2}\right|^2 \quad \text{(S-7)}$$

which estimates a very low reflectance across the air-effective medium interface and between each two EMLs of the Cu-CNT NWs structure having a very small difference in their refractive indices (see Figure S9c), in agreement with the suppressed simulated reflectance spectrum for the Cu-CNT NWs structure in Figure 4c.

The obtained relations for the effective relative permittivity of the EMLs in the CNTs coating and for the Cu-CNT NWs arrays structure were used as inputs in our numerical simulations for calculating the normalized scattering cross-section spectrum of a single Cu-CNT NW and the specular reflectance spectrum of the Cu-CNT NWs arrays structure by using COMSOL Multiphysics software. A similar procedure was employed for modeling the effective medium in Cu NWs structures.

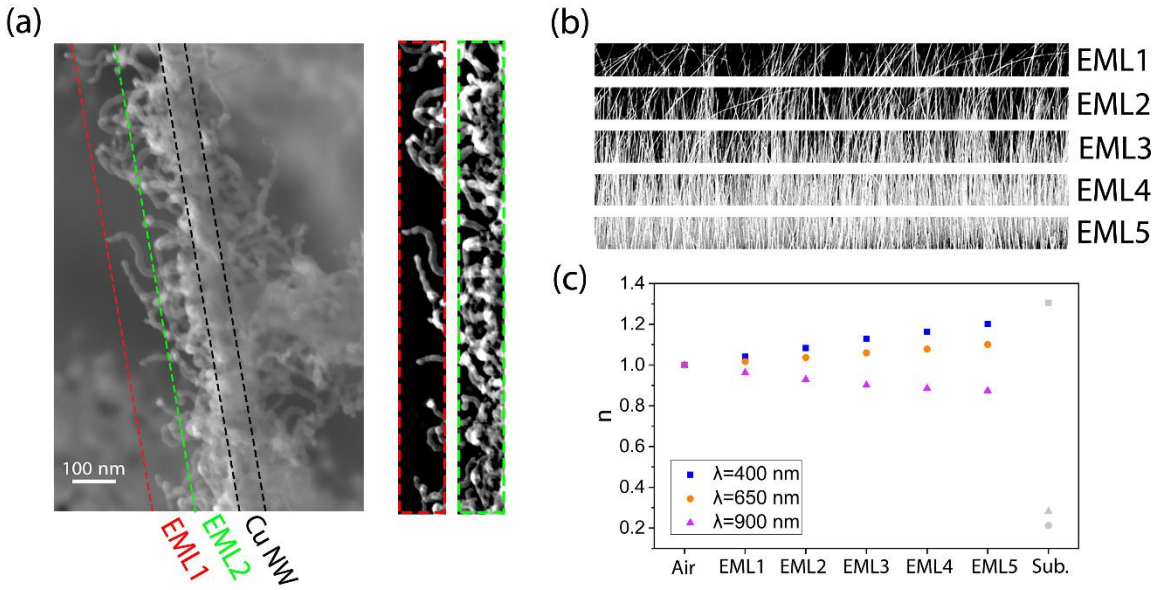

Figure S9. Image analysis results for a typical Cu-CNT NW and an array structure. (a) High-magnification SEM image of an individual Cu-CNT NW together with the volume fractions of CNTs and air in each of the two EMLs of CNTs defined by image analysis. (b) Image analysis results of the cross-sectional SEM image in **Fig. 2a** for obtaining the volume fractions of Cu NWs and air in each of the five EMLs of Cu NWs arrays. (c) real part of graded refractive index profile across the thickness of the Cu-CNT NWs structure considered as a five-layers structure of EMLs at 400, 650, and 900nm wavelengths obtained from array scale level simulations (see section S3.2.2).

Table S1. The volume fraction of Cu NWs constituent in each EMLs obtained from image analysis reported in **Fig. S9b**.

Layer	$f_{NW,i}$
EML1	0.17
EML2	0.34
EML3	0.52
EML4	0.66
EML5	0.82

S3.2 Numerical simulation

S3.2.1 Numerical Modeling of a single Cu NW and Cu-CNT NW

We developed an electromagnetic numerical method for modeling the optical properties of a single Cu NW and Cu-CNT NW on Cu substrate in COMSOL Multiphysics. For linearly polarized (LP) illumination, we modelled a 2D cut of a 3D geometry in order to maintain maximum resolution in wave propagation and scattering/reflection from the long nanowire and the Cu substrate. By solving a time-averaged wave equation as seen in eq. S.8, for an LP wave of the form of eq. S.9, we obtained a solution for a three-component electric field in the 2D computational domain.

$$\nabla \times \frac{1}{\mu_r}\left(\nabla \times \vec{\boldsymbol{E}}\right) - \ {k_0}^2 \left(\varepsilon_r - \frac{j\sigma}{\omega \varepsilon_0}\right) \vec{\boldsymbol{E}} = \vec{\boldsymbol{0}} \tag{S-8}$$

$$\vec{\boldsymbol{E}} = e^{-j\vec{\boldsymbol{k_0}}\cdot\vec{\boldsymbol{z}}}\, \hat{x} \tag{S-9}$$

This domain was bounded by a scattering boundary condition to eliminate any reflection from the boundaries. The domain covered an area of 20x40 μm while the Cu NW was 100 nm by 30 μm. Two effective carbon-air layers were added (see Figure S9a), each with 107 nm thickness in all directions. The Cu NW was modelled both in the presence of the CNT layers and as a standalone structure for both parallel and perpendicular polarizations. In all four cases, the incoming electric field was polarized perpendicular to the propagation direction (TE) while the magnetic field polarization was always set in the out-of-plane direction (TEM). Out-of-plane field propagation and polarization were not considered as they would simulate a system that describes Cu rectangles and not Cu nanowires. The system was meshed with a 0.1-12 nm resolution within the nanowire and the EMLs and with a 10-60 nm resolution close to the boundaries. For simulating the behavior of a Cu NW that was grown on a Cu substrate, we bound one end of the wire with an adjacent Cu layer that spanned to the domain boundaries. This was very important for a realistic study of the system as a close-ended resonator on the one side and as an open ended on the other.

The wavelength-dependent relative permittivity (ε_r) of copper was obtained by the work of Johnson and Christy[10] and the relative magnetic permeability (μ_r) was set as 1 without loss of generality in all computational domains. The EMLs of CNTs were given weighted ε_r values for 65% carbon[11] and 35% air (ε_r =1) for the EML in contact with the nanowire and 25% carbon and 75% air for the outer EML according to what was described in the previous section. The surrounding medium was considered to be air (ε_r =1).

The resulting bi-dimensional solution for the electric field was exploited to integrate over the Cu domain area for the energy rate absorbed, found in eq. S10. Similarly, it was also exploited to integrate over a closed loop that surrounds the Cu nanowire (and the nanowire-EML system) for the energy rate scattered, found in eq. S11. Accordingly, both were divided by the incident irradiance (eq. S12) to obtain the absorption and scattering cross-sections (eq. S13).

$$W_{Abs} = \frac{1}{2}\iiint_{xyz} \left[\mathrm{Re}\left[(\sigma \vec{E} + j\omega \vec{D}) \cdot \vec{E}^{*}\right] + j\omega \vec{B}) \cdot \vec{E}^{*} \right] \mathrm{dxdydz} \quad [W] \tag{S-10}$$

$$W_{sca} = \oiint \left[\vec{E} \times \vec{H}^{*}\right] \cdot \mathbf{n}\mathrm{dS} \quad [W] \tag{S-11}$$

$$P_{incident} = \frac{1}{2Z_0}\left|\overrightarrow{E_0}\right|^2 \quad [W/m^2] \tag{S-12}$$

$$\sigma_{Abs} = \frac{W_{Abs}}{P_{incident}} \quad [m^2] \qquad \sigma_{Sca} = \frac{W_{Sca}}{P_{inc}} \quad [m^2] \tag{S-13}$$

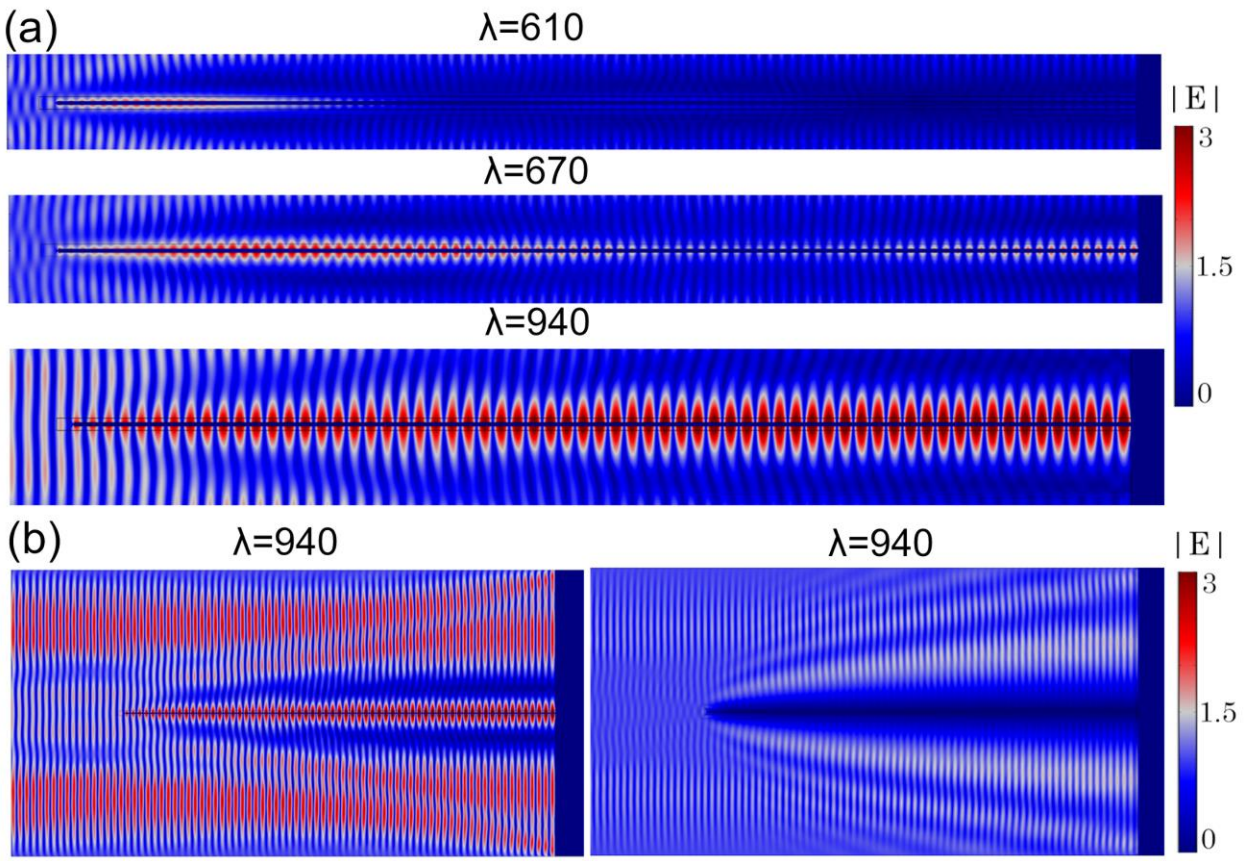

Figure S10. The corresponding electric field norm plots of the normalized scattering spectra shown in **Figure 4a** for propagation parallel to the long axis of the NW and polarization perpendicular to it. (a) Electric field norm plots of the three envelope resonant modes of a 30µm-long single Cu NW on Cu substrate at 610, 670, and 950nm wavelengths. (b) Electric field norm plots of scattering for a single Cu NW (left) and a Cu NW covered with two EMLs of CNTs (right, see **Figure S9a**) on Cu substrate at 950nm wavelength.

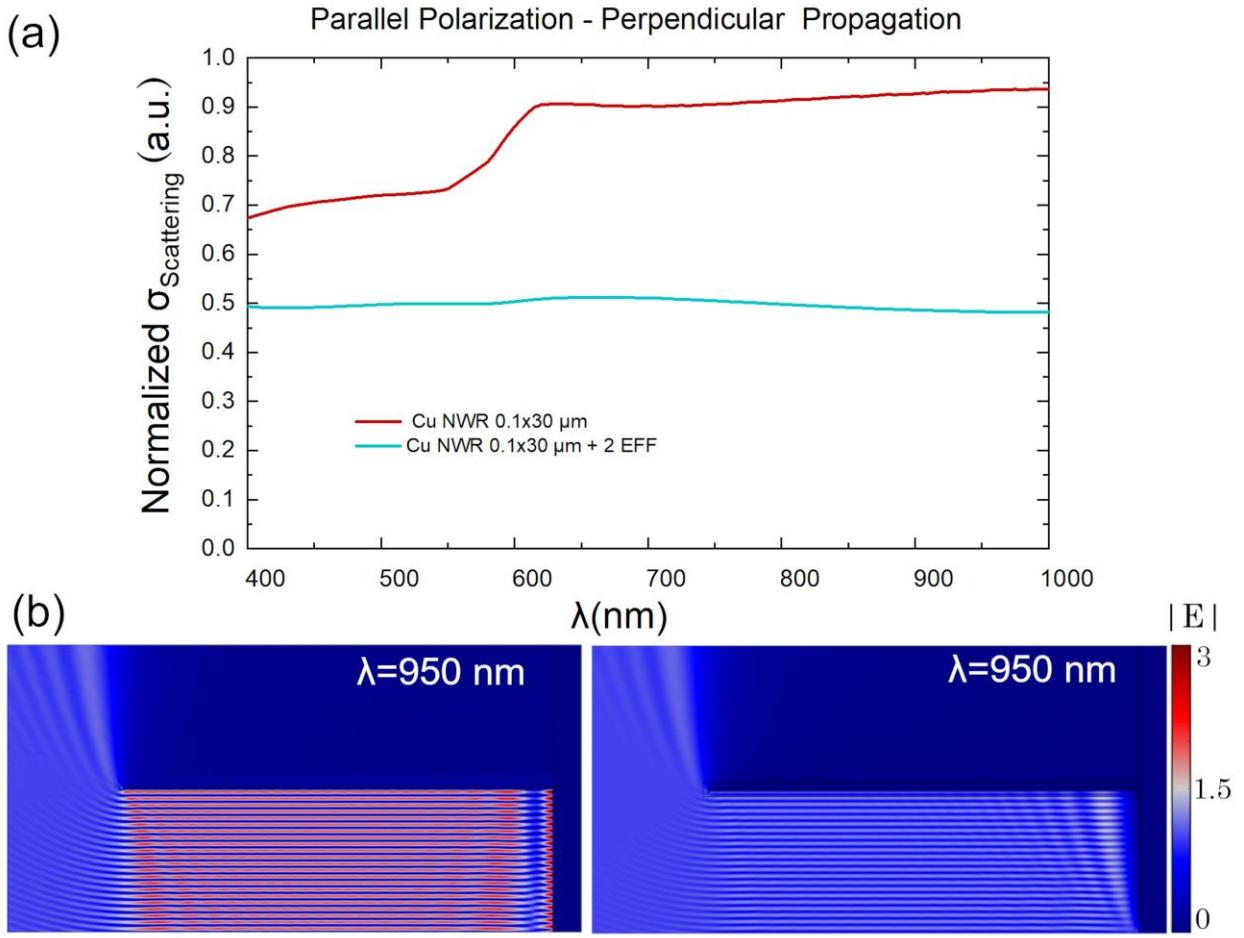

Figure S11. (a) the simulated normalized scattering spectra, and (b) the corresponding electric field norm plots for a 30µm-long Cu NW (left) and a Cu NW covered with two EMLs of CNTs (right, see **Figure S9a**) on Cu substrate at 950 nm wavelength for propagation perpendicular to the long axis of nanowire and polarization parallel to it.

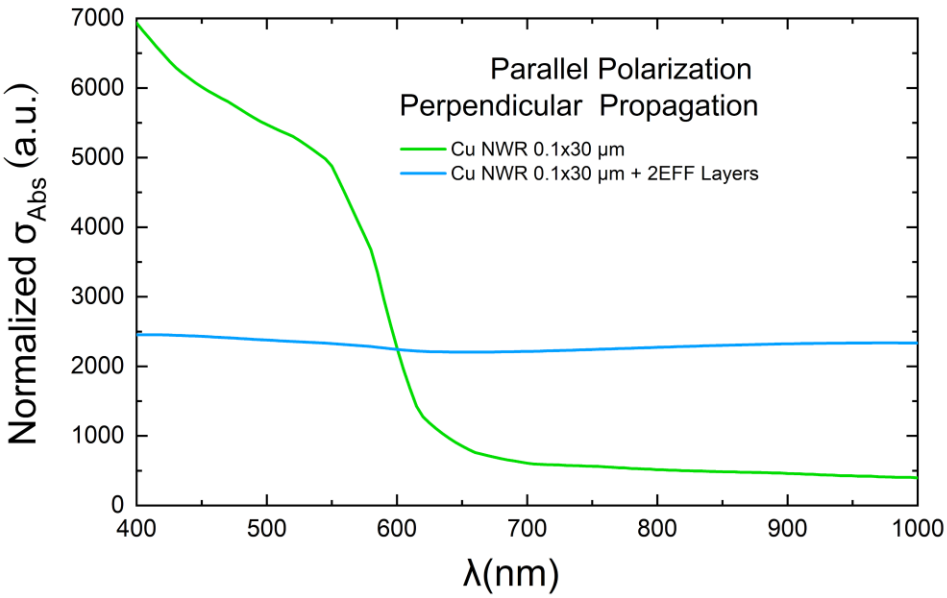

Figure S12. Absorption cross section spectra for a single Cu NW and a Cu NW covered with two EMLs of CNTs on a Cu substrate in comparison for propagation perpendicular to the long axis of nanowire and polarization parallel to it.

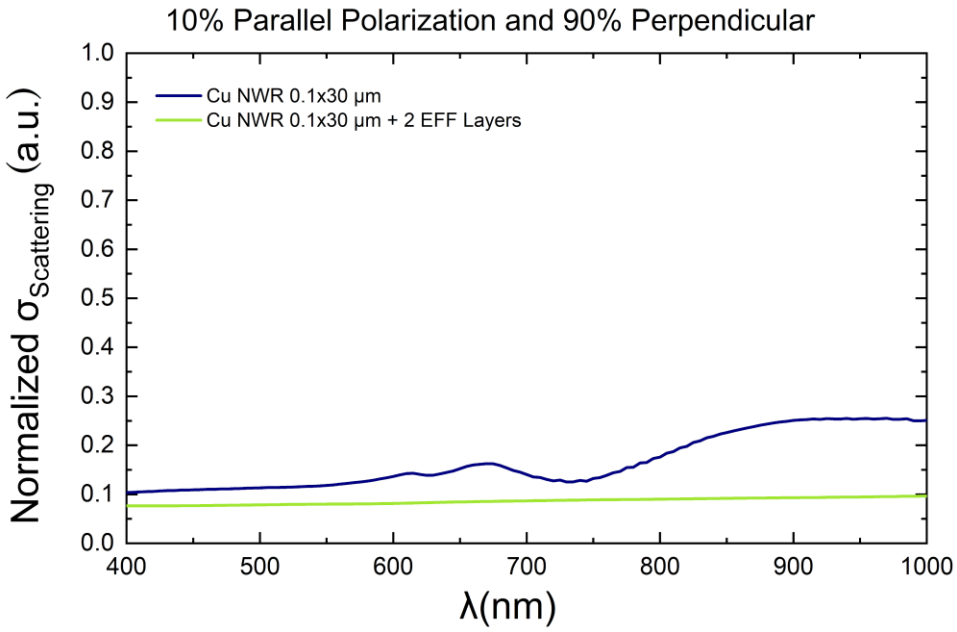

Figure S13. Weighted-average scattering spectra for a single Cu NW and a Cu NW covered with two EMLs of CNTs on a Cu substrate, assuming 10% contribution from an incoming wave propagating perpendicular to the nanowire axis and 90% contribution from an incoming wave propagating parallel to the wire axis.

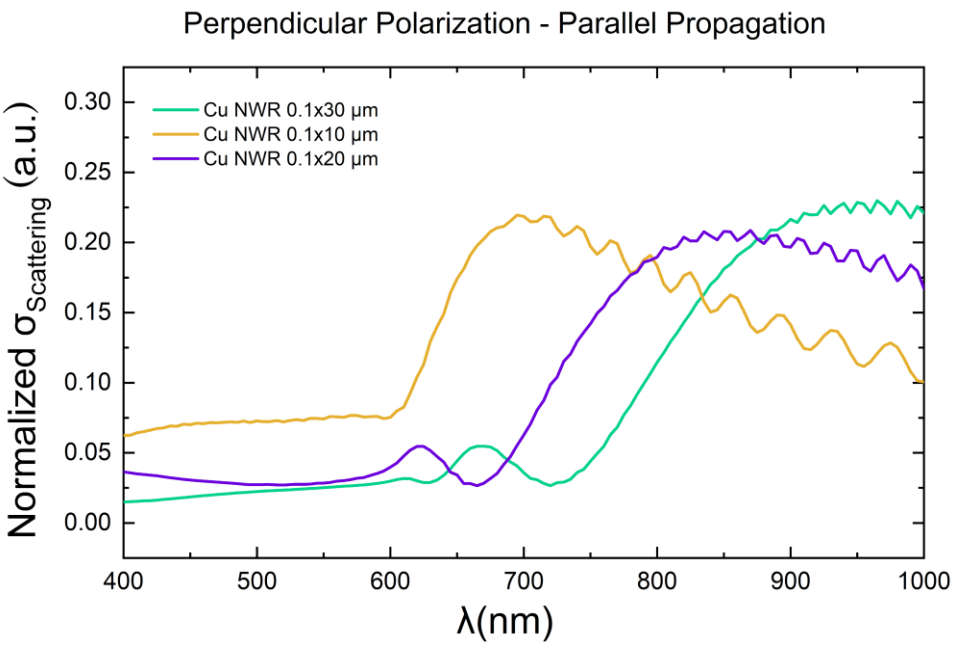

Figure S14. Normalized scattering cross-section spectra of standalone Cu NWs on Cu substrate having different lengths of 10, 20, and 30µm for propagation parallel to the long axis of the nanowire and polarization perpendicular to it.

S3.2.2 Numerical Modeling of nanowire array structures

To model the optical properties of EMLs-equivalent of the Cu NWs and Cu-CNT NWs array structures as well as a free-standing Cu film, we performed frequency domain electromagnetic full field calculations in COMSOL Multiphysics. In particular, we used a 2D unit cell model with periodic and port boundary conditions. In this approach, Maxwell's equations (eq. S-8 and S-9) are converted to matrix equations which are solved by using direct or iterative methods, and the reflectance of each structure is calculated by the scattering parameters of the periodic unit cell.

The unit cell consisting of the NW array structure (Cu NWs or Cu-CNT NWs) on Cu substrate surrounded with two top and bottom layers of air. The height and width of the unit cell were equal to 32µm and 200nm, respectively. As explained in section S.3.1, to represent the NWs array structures we defined five graded EMLs of NWs with an overall height of 30µm, each with an effective relative permittivity retrieved from the reported volume fractions in Table S.1 and eq. S-5 and S-6 for the Cu NWs and Cu-CNT NWs arrays, respectively. At the side walls of the unit cell, Floquet periodic boundary condition was assumed to simulate infinite-size multilayer film structures. At the top and bottom of the unit cell, we set a port

boundary condition for excitation and reflection calculations. Each structure was illuminated normally from the top by a 1V/m plane wave (400 to 1000nm) with polarization parallel to the film. The reflectance was automatically calculated from the reflected power from the port 1 (S_{11}) at the top of the unit cell according the following relation:[9,12]

$$R = |S_{11}|^2 \quad \text{(S-14)}$$

References

(1) Mashock, M.; Yu, K.; Cui, S.; Mao, S.; Lu, G.; Chen, J., Modulating gas sensing properties of CuO nanowires through creation of discrete nanosized p–n junctions on their surfaces. *ACS Appl. Mater. Interfaces* **2012,** *4* (8), 4192-4199.
(2) Han, J.-W.; Lohn, A.; Kobayashi, N. P.; Meyyappan, M., Evolutional transformation of copper oxide nanowires to copper nanowires by a reduction technique. *Mater. Express* **2011,** *1* (2), 176-180.
(3) Du, L.; Shi, T.; Su, L.; Tang, Z.; Liao, G., Hydrogen thermal reductive Cu nanowires in low temperature Cu–Cu bonding. *J. Micromech. Microeng.* **2017,** *27* (7), 075019.
(4) Rashid, N. M.; Kishi, N.; Soga, T., Effects of reduction temperature on copper nanowires growth by thermal reduction of copper oxide nanowires. *Mod. Phys. Lett. B* **2016,** *30* (17), 1650193.
(5) Atthipalli, G. Growth of Aligned Carbon Nanotubes on Copper Substrates. University of Pittsburgh, 2011.
(6) Cao, F.; Jia, S.; Zheng, H.; Zhao, L.; Liu, H.; Li, L.; Zhao, L.; Hu, Y.; Gu, H.; Wang, J., Thermal-induced formation of domain structures in CuO nanomaterials. *Phys. Rev. Mater.* **2017,** *1* (5), 053401.
(7) Kurvits, J. A.; Jiang, M.; Zia, R., Comparative analysis of imaging configurations and objectives for Fourier microscopy. *JOSA A* **2015,** *32* (11), 2082-2092.
(8) Karadan, P.; Anappara, A. A.; Moorthy, V.; Narayana, C.; Barshilia, H. C., Improved broadband and omnidirectional light absorption in silicon nanopillars achieved through gradient mesoporosity induced leaky waveguide modulation. *RSC Adv.* **2016,** *6* (110), 109157-109167.
(9) COMSOL, A., COMSOL Multiphysics Reference Manual: Version 3.5. Stockholm: 2008.
(10) Johnson, P. B.; Christy, R.-W., Optical constants of the noble metals. *Phys. Rev. B* **1972,** *6* (12), 4370.
(11) Djurišić, A. B.; Li, E. H., Optical properties of graphite. **1999,** *85* (10), 7404-7410.
(12) Hesthaven, J. S., Time-domain finite element methods for Maxwell's equations in metamaterials. *SIAM REV* **2014,** *56* (ARTICLE), 202-203.